JMEPEG (2024) 33:7054–7073
https://doi.org/10.1007/s11665-023-08482-4

1059-9495/$19.00

ORIGINAL RESEARCH ARTICLE

Laser Surface Modification of Single-Crystal Nickel-Based Superalloy: Geometry, Microstructure, Crack Morphology, and Microhardness

Srinivasa Rao Nandam, A. Venugopal Rao, Amol A. Gokhale, and Suhas S. Joshi

Submitted: 22 January 2023 / Revised: 7 May 2023 / Accepted: 20 May 2023 / Published online: 13 July 2023

The present work investigates the surface modification of a second-generation, SX nickel-based superalloy by using a continuous wave laser with various laser powers under the conductive mode of heat penetration. The aim was to reduce the surface strength to improve the machinability. The results show that the laser surface modified (LSM) geometry and their surface irregularities increase with an increase in laser power. The cross section of the LSM geometry under lower powers is semi-elliptical in shape, whereas it becomes a top-hat shape under higher laser powers. Fine dendrites of around 10 μm with various morphologies are formed in the LSM geometry. The dendrite size increases with an increase in laser power except at the highest laser power. The LSM geometry consists of longitudinal and transverse cracks along the scanning direction. The longitudinal cracks are formed near the centerline at lower laser powers, whereas the transverse cracks are formed at a faraway distance from the centerline at higher laser powers. The longitudinal cracks have vertical cracking and transverse cracks have zig-zagged cracking beneath the surface. The total crack length increases with an increase in laser power. The LSM interface consists of dense micropores and microcracks at the inter-dendric region. However, the LSM region consists of lesser microsegregation and fine dendrites than the base metal, its microhardness is lower than the base metal due to the formation of laser-induced defects.

Keywords crack morphology, laser power, laser surface modification, microhardness, microstructure, single-crystal nickel-based superalloy

1. Introduction

Nickel-based superalloys are one of the prominent materials that can withstand thermal loads up to 80% of the melting temperature of the alloy in service. Therefore, components made from nickel-based superalloy are exclusively used in the hot sections of advanced gas turbine engines in aerospace and power generation applications (Ref 1). The advanced cast, single-crystal (SX) castings result in superior turbine engine performance and durability by offering improved creep-rupture, fatigue, oxidation, and coating properties over equiaxed and columnar-grained castings due to the absence of low melting grain boundary constituents, superior alloy chemistry and a high-volume fraction of γ' precipitates (Ref 2).

During the application of SX nickel-based superalloys in manufacturing turbine blades, significant material removal is necessary. But, nickel-based superalloys are often considered as 'difficult-to-machine' materials owing to their high strength, hot hardness, severe work hardening, and low thermal conductivity (Ref 3). During their machining high cutting forces and heat are generated, which result in the premature failure of cutting tools, lower material removal rate, and poor integrity of machined surfaces (Ref 4). Therefore, sophisticated machinery, special tools, and techniques are often employed for machining these alloys. A few researchers are working on developing alternative machining processes such as non-traditional machining, laser-assisted machining, and hybrid machining to assess their viability (Ref 5). Nickel-based superalloys show an increase in the flow stress with an increase in temperature up to about 650 °C due to Kear Wilsdorf lock by cross slip (Ref 6). Therefore, the material will not soften using normal heating techniques. But SX nickel-based superalloys are highly susceptible to cracking under remelting due to extended solidification temperature. In addition, a large grain-sized material shows more cracking than a small grain-sized material due to reduced ductility in them.

Laser surface modification (LSM) is one of the emerging technologies for controlled surface modification on advanced materials (Ref 7). Continuous wave (CW) solid-state lasers are more prominently used in the laser processing of engineering materials due to their high energy efficiency, beam quality, modularity, and serviceability. Ruppik et al. (Ref 8) observed that high-power CW fiber lasers have superior qualities in terms

Srinivasa Rao Nandam, Department of Mechanical Engineering, IIT Bombay, Powai, Mumbai, India; and Defence Metallurgical Research Laboratory (DMRL), DRDO, Kanchanbagh, Hyderabad, India; **A. Venugopal Rao**, Defence Metallurgical Research Laboratory (DMRL), DRDO, Kanchanbagh, Hyderabad, India; **Amol A. Gokhale**, Department of Mechanical Engineering, IIT Bombay, Powai, Mumbai, India; and **Suhas S. Joshi**, Department of Mechanical Engineering, IIT Bombay, Powai, Mumbai, India; and Department of Mechanical Engineering, IIT Indore, Simrol, Indore, India. Contact e-mail: srinivas-nandam.dmrl@gov.in.

of brightness, optical-to-optical efficiency, compact design, robustness, and scalability. Although high-power CW lasers are being used in the processing of engineering materials, limited work has been reported on SX nickel-based superalloys.

A few relevant research publications found in the open literature on the surface modification of SX nickel-based superalloys by using CW fiber laser are briefly presented as follows: Anderson et al. (Ref 9) found stray grains increase with increasing CW laser power from 120 to 250 W in laser welds of CMSX-4 alloy. This could be due to a decrease in thermal gradient. Yao et al. (Ref 10) observed that the stray grains formation was due to compositional segregation under laser re-melting experiments on the 1st generation SX nickel-based superalloy (SRR 99). They used a laser power of 1 kW, scanning velocity of 5 mm/s, and beam diameter of 2 mm. Basak et al. (Ref 11) found the formation of fine planar, columnar, and equiaxed grains along with certain eutectic compounds in additively fabricated CMSX-4 deposits by scanning laser epitaxy process with 1 kW Ytterbium fiber laser of 40 μm beam diameter. Boris et al. (Ref 12) found cracks, disordered microstructure, and pores in the clad deposits on CMSX-4 superalloy using a solid-state diode laser of power of 250 W with a fiber diameter of 400 μm and a scan speed of 3.3 mm/s. Zhou et al. (Ref 13) observed that the crack propagation is a strong function of the misorientation angles of the grain boundaries in a Re-free, SX nickel-based superalloy alloy fabricated by laser powder deposition with Yb-fiber laser of 250 W at a scanning speed of 8 mm/s. Rudolf et al. (Ref 14) found solidification cracks attribute to the obstructed shrinkage in the 2nd generation, SX nickel-based superalloy (ZhS32) in laser cladding using laser power of 334 W and traverse speed of 6.7 mm/s with a beam diameter of 0.9 mm. It was understood that the laser-induced surface damage mechanisms of SX nickel-based superalloys are very complex, and they are highly dependent on both the initial condition of the work material and the subsequent laser processing parameters.

In this work, a novel concept of creating laser-induced surface damage on a SX nickel-based superalloy prior to the machining process is being investigated in the context of improving machinability. The objective is to investigate the surface modification of a SX nickel-based superalloy, particularly to the laser-induced surface defects created due to the exposure by a CW fiber laser in the conductive mode of heat penetration. In addition, the geometry, microstructure, crack morphology, elemental analysis, and microhardness in the LSM region were also investigated in detail to get the process parameter-structure and property relationships.

2. Materials and Methods

2.1 Work Material and Specimen Preparation

The CMSX-4 alloy is a rhenium-bearing, second-generation, SX nickel-based superalloy. It maintains ultra-high strength even at high temperatures (1100 °C) by virtue of solid solution strengthening and precipitation hardening. The physical and mechanical properties of CMSX-4 alloy are shown in Table 1. The alloy contains many refractory elements (Mo, Ta, W, Re) and a high amount ($>$ 6 Wt.%) of Al + Ti elements. The nominal chemical composition of CMSX-4 alloy in weight percent (wt.%) is shown in Table 2 (Ref 19).

A solid block was extracted by a precision WEDM (wire electric discharge machining) process from the top mold region of SX casting, it was fabricated with near $<$ 001 $>$ grain growth direction using prefix bottom seeding and directional solidification techniques in a vacuum investment casting process. To ensure high dimensional accuracy and remove surface defects related to WEDM, the SX specimens underwent gentle grinding on all surfaces. The specimens were of a length of 40 mm, a width of 16 mm, and a thickness of 13 mm and were having a flatness ranging from 20 to 30 μm, and an average surface finish of 0.2 μm Ra, on the top and bottom sides.

2.2 Experimental Setup

A precision CNC (computer numerically controlled) laser welding machine, fabricated by M/s Arnold Ravensburg, Germany was used for LSM experiments. The machine consisted of four major subsystems, namely high-power CW fiber laser, optical head, argon gas shielding system, and workpiece positioning system. The CW fiber laser system (model of FL040 from M/s Rofin-SINAR Laser GmbH, Hamburg, Germany), had a neodymium ytterbium-doped solid-state laser with an average output power of 4 kW + 1%, a wavelength of 1070 + 10 nm, and a pulse modulation frequency of 5 kHz. The output of 4 kW was achieved by the integration of four numbers of 1 kW single-mode fibers (Ref 20). The laser system was coupled to the optical head by an optical fiber with a core diameter of 200 μm. The optical head had collimation optics and a longer focal length focusing optics to deliver the laser beam of 440 μm. The optical head moves in three linear directions within 2500 mm $\times$ 3000 mm $\times$ 750 mm, besides two rotary directions over a gantry-type CNC arrangement. The argon gas shielding system consisted of multiple gas nozzles externally fitted to the optical head for supplying the necessary shielding gas over the test specimens. The workpiece position system consisted of a fixed horizontal table with mounting and fixturing arrangements to hold the test specimens firmly. A picture of the experimental setup used for the LSM is shown in Fig. 1(a).

2.3 Experimental Parameters and Procedure

A positive focus shift was maintained to get a defocused laser beam and thereby obtain a bigger beam diameter to avoid the key-hole mode of beam penetration. Several trial experiments were performed on the test specimens with varying laser power for obtaining a suitable working range of power levels for melting the work surface. The energy density was calculated as a ratio of laser power and the product of scan speed and beam diameter. The parameters selected for the LSM experi-

Table 1 The physical and mechanical properties of CMSX-4 alloy

Parameter	Unit	Value	Reference
Density	Kg/m^3	8700	(Ref 15)
Thermal conductivity at RT	W/m/K	8	(Ref 15)
Melting temperature	°C	1326-1385	(Ref 16)
Coefficient of thermal expansion @ 800 °C	μm/m / ° C	15	(Ref 17)
Specific heat at RT	J/Kg/K	351	(Ref 15)
Latent heat of fusion	J/g	231 ± 13	(Ref 18)
Yield strength @760 °C	MPa	980	(Ref 15)
Ultimate Tensile Strength @760 °C	MPa	1200	(Ref 15)
Elongation @760 °C	%	10	(Ref 15)

Table 2 The nominal chemical composition of, CMSX-4 alloy in wt.%

Cr	Co	Mo	Ti	Al	W	C	Ta	Re	Hf	Ni
6.5	9.6	0.6	1.0	5.6	6.4	0.05	6.5	3.0	0.1	Balance

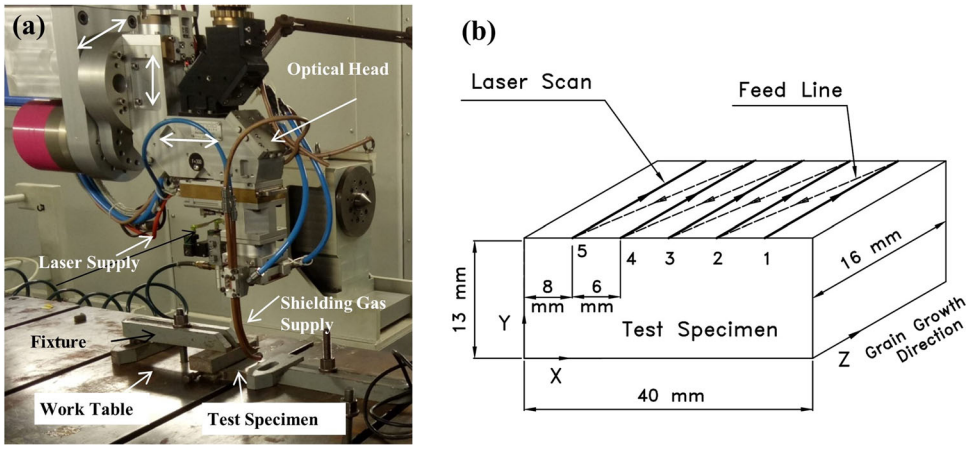

Fig. 1 The experimental setup for the LSM on a SX nickel-based superalloy (a) a photograph of the experimental setup, and (b) a schematic of the unidirectional laser scanning path

Table 3 Processing parameters for LSM on CMSX-4 alloy

Parameter	Unit	Value				
Scan	…	1	2	3	4	5
Laser power	W	500	750	1000	1250	1500
Scan speed	mm/s	5.5	5.5	5.5	5.5	5.5
Beam diameter	mm	0.93	0.93	0.93	0.93	0.93
Heat input	J/mm	91	136	182	227	273
Energy density	J/mm^2	98	147	196	244	293

ments are shown in Table 3. High-purity argon at a flow rate of 10 *lpm* at atmospheric pressure under room temperature was used as a shielding gas during the process to avoid oxidation and reflection of metallic flumes into the optical head. A fixed offset distance of 6 mm was maintained between the successive laser tracks to avoid overlapping of the LSM geometries. The LSM was performed along the unidirectional scan paths as shown in Fig. 1(b) by developing CNC part programs.

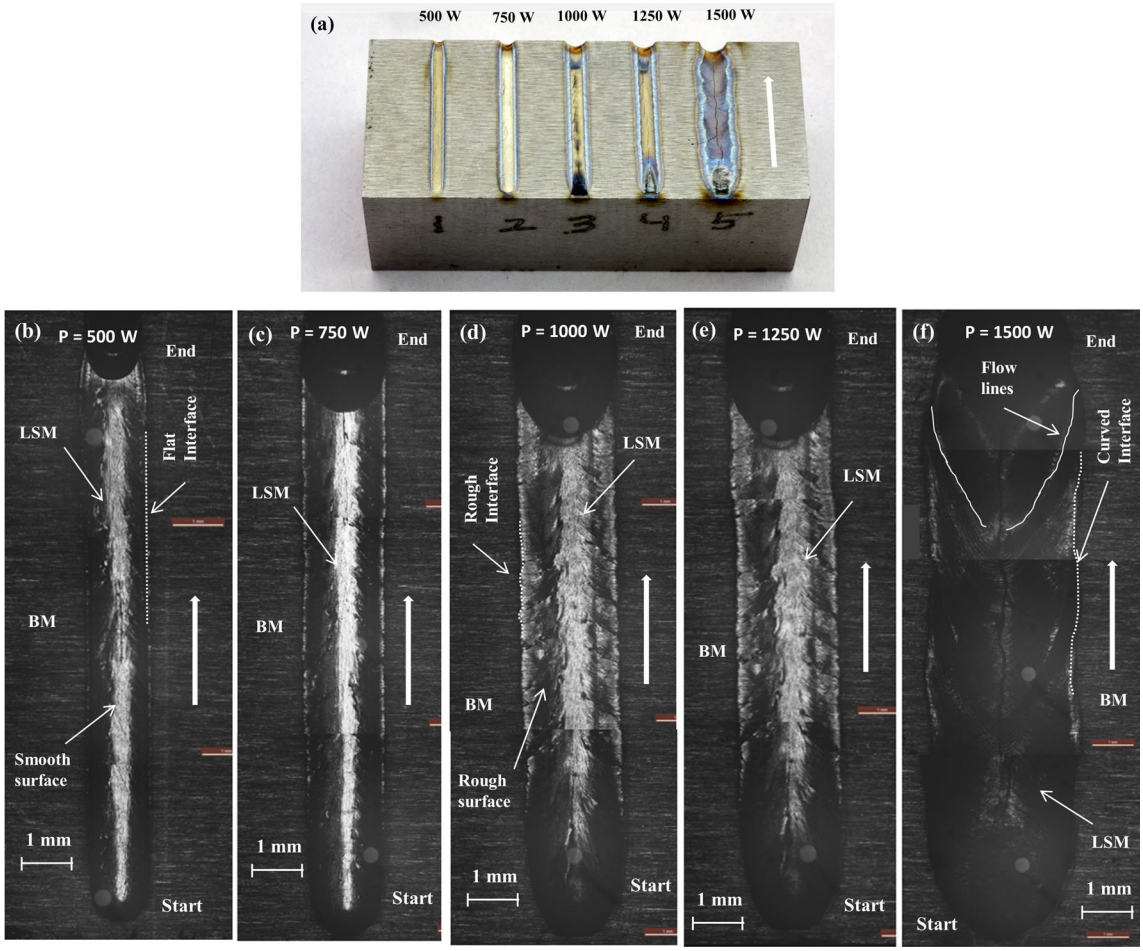

Fig. 2 Plan view of the LSM geometries of a SX nickel-based superalloy (a) test specimen, and (b) to (f) magnified optical micrographs (12.5 x) corresponding to the laser power of 500, 750, 1000, 1250, and 1500 W, respectively, under a scan speed of 5.5 mm/s

2.4 Characterization Techniques

The laser surface-modified geometries of the specimen were extracted by precision cutting across the scan lengths using the WEDM process at 6 mm from the start of the laser scan to avoid the ramping effect. The samples were placed in Bakelite molds and polished using a combination of emery papers, diamond paste, and common metallographic methods followed by dip etching with Kalling's 2 reagent to examine the complete cross-sectional view of the LSM region. The micro-structural analysis was carried out using an optical microscope and a scanning electron microscope (SEM). The SEM image analysis was carried out under the back-scattered secondary electron (BSE) technique to get high-contrast images. The dimensional measurements of the LSM geometry, dendrites and crack morphologies in the LSM were carried on their digital micrographs by using an image processing software, Image J. The interface profiles of LSM geometries were captured by using a video measuring microscope (VMM). The chemical analysis was carried out by using the energy-dispersive x-ray spectroscopy (EDS) technique of SEM for the elemental composition. The strength of the LSM geometries was assessed by measuring the surface hardness using a high-precision Vickers micro-hardness tester. A diamond pyramid indenter was used under a 500 g load with a dwell time of 10 seconds.

3. Results and Discussion

3.1 Laser Surface Modified Geometry

The SX nickel-based superalloy specimen with LSM geometries created under various laser power levels is shown

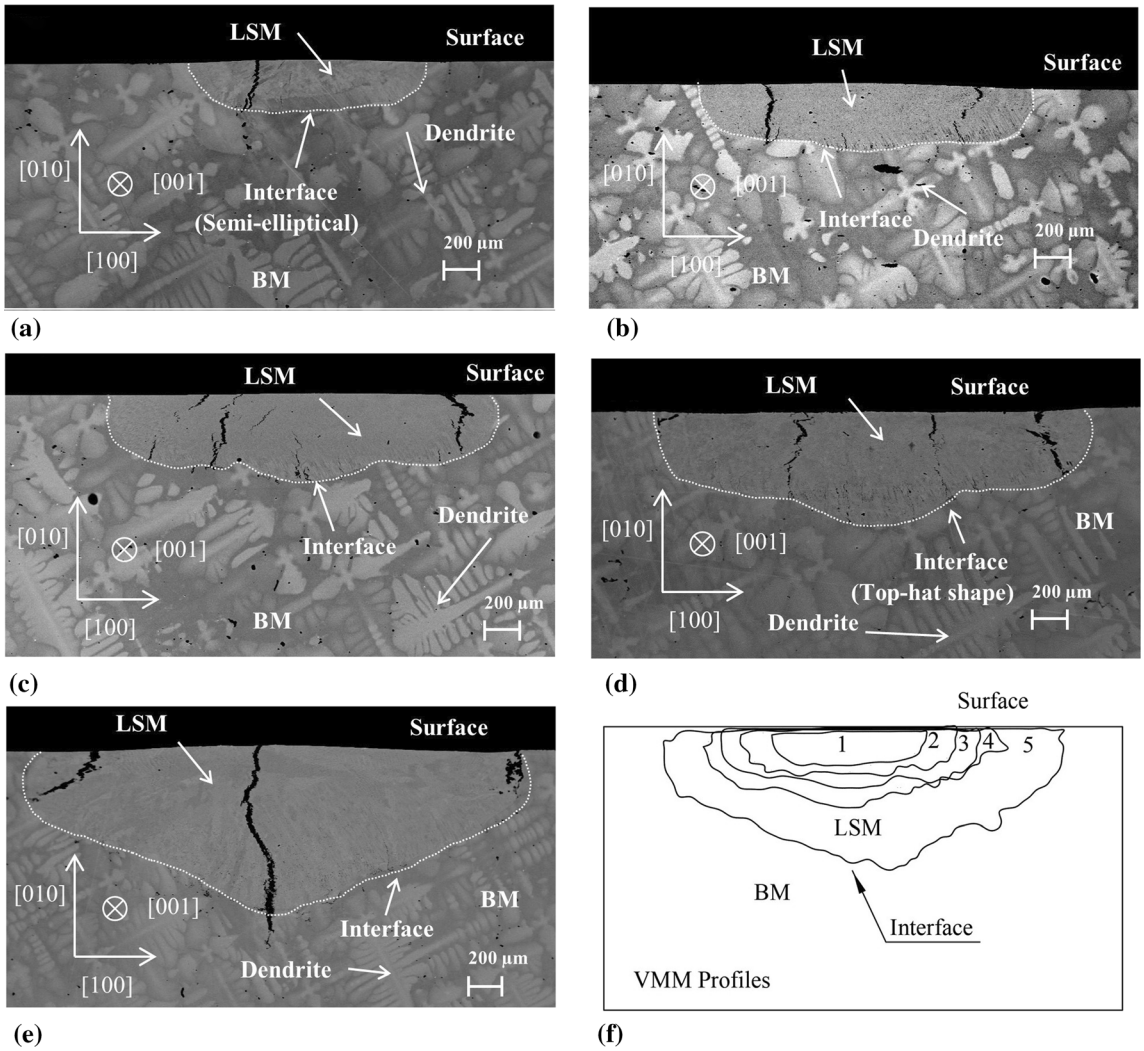

Fig. 3 Low magnification (100 x) SEM micrographs of the cross section of the LSM geometry corresponding to the laser power of (a) 500, (b) 750, (c) 1000, (d) 1250, and (e) 1500 W, and (f) superimposed LSM interface profiles of various laser powers

in Fig. 2(a). The magnified optical micrographs of the plan view of the LSM geometries corresponding to the laser power ranging from 500 to 1500 W are shown in Fig. 2(b), (c), (d), (e), and (f). It is observed that the LSM geometries are straight along the vertical direction due to the high accuracy of the employed laser welding machine. The LSM surfaces are smoother when using lower laser power, whereas the surfaces are rougher with intermediate and high-power levels. The interface between the LSM and base metal (BM) is flat (shown as a dotted white line in Fig. 2b) at the lowest power, whereas the interface has a curved profile at intermediate and high-power levels. A higher laser power results in the melting of a larger volume of BM due to high supply energy. The remelting of LSM geometry at higher laser power could cause rough surfaces along the scan length. Curved flow lines from the interface to the centerline of LSM in opposite to the scanning direction are visible on the surface under the highest laser power (shown with a solid white line in Fig. 2f). In general, the melt pool starts solidification from the interface to the centerline (middle) of the LSM geometry perpendicular to the scanning direction under a steady state. The observed curved flow line could be due to the variation in solidification pattern as the solidification starts at the interface and ends at the middle of LSM geometry a far way distance opposite to the scanning direction by the scan speed. The high laser power also results in the melting of higher BM. The high thermal energy under low

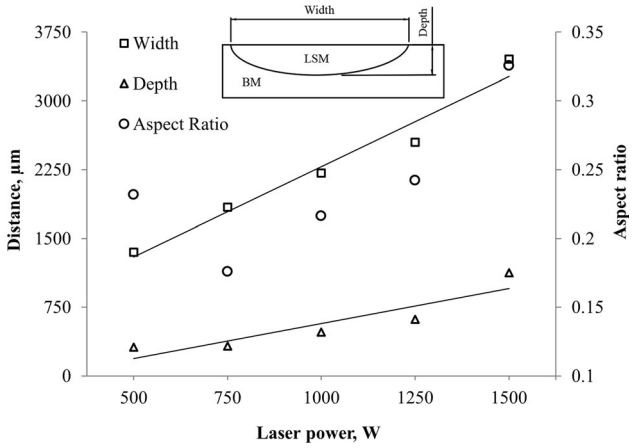

Fig. 4 Dimensions of the LSM geometry such as maximum width, depth, and aspect ratio as a function of laser power of a SX nickel-based superalloy under a scan speed of 5.5 mm/s and a beam diameter of 0.93 mm

thermal conductivity of BM results in a low thermal gradient, in turn, it results in slow solidification. The melt pool under long solidification time experiences melting pool instabilities. The observed surface undulations such as rough surfaces, curved interfaces, and flow lines of the LSM under high laser power could be also attributed to the instability of the melt pool. Similar observations were made by Qiu et al. (Ref 21) in the selective laser melting of titanium superalloys. The researchers suggested that the Marangoni forces and recoil pressure were the main reasons for causing the instabilities in the melt flow, that caused high surface undulations. Smooth surfaces and flat interfaces of LSM observed under lower power could be due to the rapid solidification of the melt pool, such that it does not get sufficient time to generate surface undulations.

The SEM micrographs of the cross section of the LSM geometries embedded with the direction of the laser scanning [001] under various laser powers are shown in Fig. 3(a), (b), (c), (d), and (e). It is observed that the LSM consists of a significant area beneath the surface without any visible dendrites. The BM outside the interface, however, shows a coarse dendritic microstructure. The interfaces were shown with the white dotted curve in the figures. A sharp interface is indicative of a narrow HAZ, which could be a result of a highly concentrated laser beam and steeper thermal gradients commonly observed in laser materials processing (Ref 22). The LSM geometry under lower powers is semi-elliptical in shape, whereas the LSM geometry under high powers is observed to have a top-hat shape. This could be due to a change in the operating mode of the laser from single to multimode under higher laser power.

The interface profiles extracted from the LSM geometries by using the VMM are superimposed on each other, see Fig. 3(f). It is observed that the area of LSM geometry increases with an increase in laser power due to an increase in the supply of heat energy. It is also observed that the LSM geometries under laser power from 500 to 1250 W show larger width and shallow depth due to the conductive mode of heat penetration, whereas the LSM geometry under laser power of 1500 W shows a comparatively deeper depth due to the transition mode of penetration. The dimensions of LSM geometries such as maximum width, depth and aspect ratio (depth to width) as a function of the laser power are shown in Fig. 4. It is observed that an increase in laser power increased both the width and depth of the LSM geometry. The aspect ratio ranging from 0.18 to 0.33 exhibits a decrease and increasing trend with a minimum of 750 W. A comparatively higher aspect ratio at a lower laser power of 500 W could be due to the low penetration of a bigger beam diameter on the work material.

3.2 Microstructural Changes

3.2.1 LSM Region. The identified location on the cross section of the LSM geometry adjacent to the solidification cracks for high magnification (5000 x) SEM analysis is shown in Fig. 5(a). The SEM micrographs under various laser powers ranging from 500 to 1500 W are shown in Fig. 5(b), (c), (e), and (f). The LSM region has fine dendritic microstructures with various morphologies and orientations. The dendrites observed under lower laser powers up to 750 W are finer, 4-8 μm in size, whereas they are slightly coarser, 10 to 20 μm in size under laser powers of above 750 W. The different shapes of dendrites were observed, these include round-rectangular, equiaxed, Ginger, Christmas tree, turbine disk, and flying bird under the laser power from 500 W to 1500 W. The size of the primary and secondary arm lengths of the dendrites as a function of the laser power is presented in Fig. 5(g). The length of both the primary dendrite arm (PDA) and secondary dendrite arm (SDA) increases with an increase in the laser power except at 1500 W, where the length of PDA decreases steeply. A change in mode at the highest laser power was permitted to nucleate multiple dendrites under a bigger cross-sectional area. Therefore, multiple dendrites could grow up to a certain size during the solidification. Solid diffusion depends on the cooling rate and the dendritic arm length. The cooling rate in the LSM region can be estimated by knowing the SDA length as given by (Ref 23):

$$SDA = \frac{A}{V^n} \quad \text{(Eq 1)}$$

where V is the cooling rate, A and n are material constants. Meharabian et al. (Ref 24) calculated the values of A and n for a nickel-based superalloy, Inconel 718 as 141, and 0.4, respectively. The calculated cooling rates from the measured SDA as a function of laser power are shown in Fig. 5(h). It is observed that the cooling rate decreases with an increase in laser power except at 1500 W. Pores of size ranging from

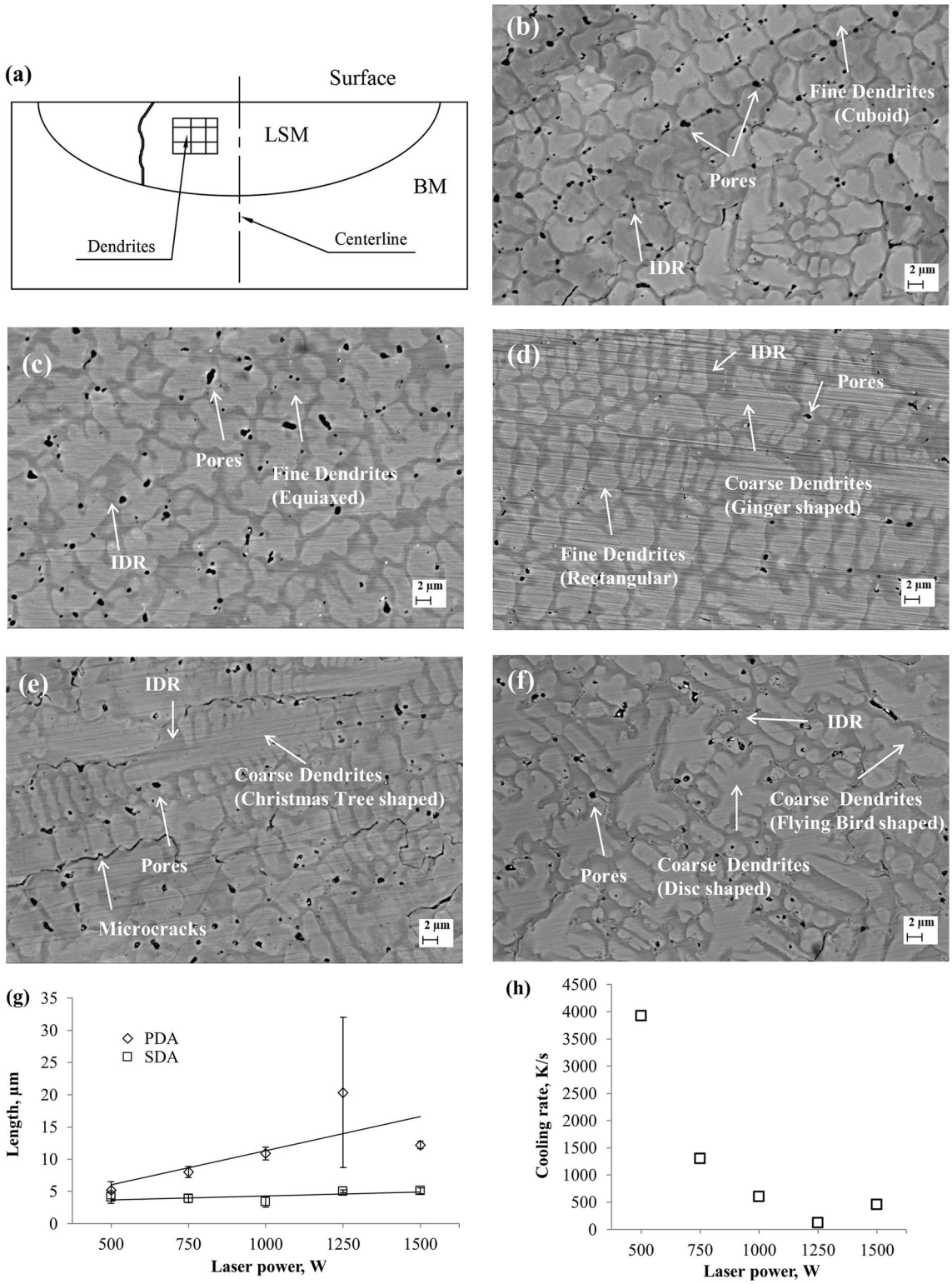

Fig. 5 Microstructure of the LSM region, (a) a schematic of the location identified on the cross section of LSM geometry for high magnification SEM analysis, and (b) to (f) micrographs (5000 x) corresponding to laser powers of 500, 750, 1000, 1250, and 1500 W (g) primary and secondary dendritic arm lengths, and (h) cooling rate as a function of laser power under a scan speed of 5.5 mm/s

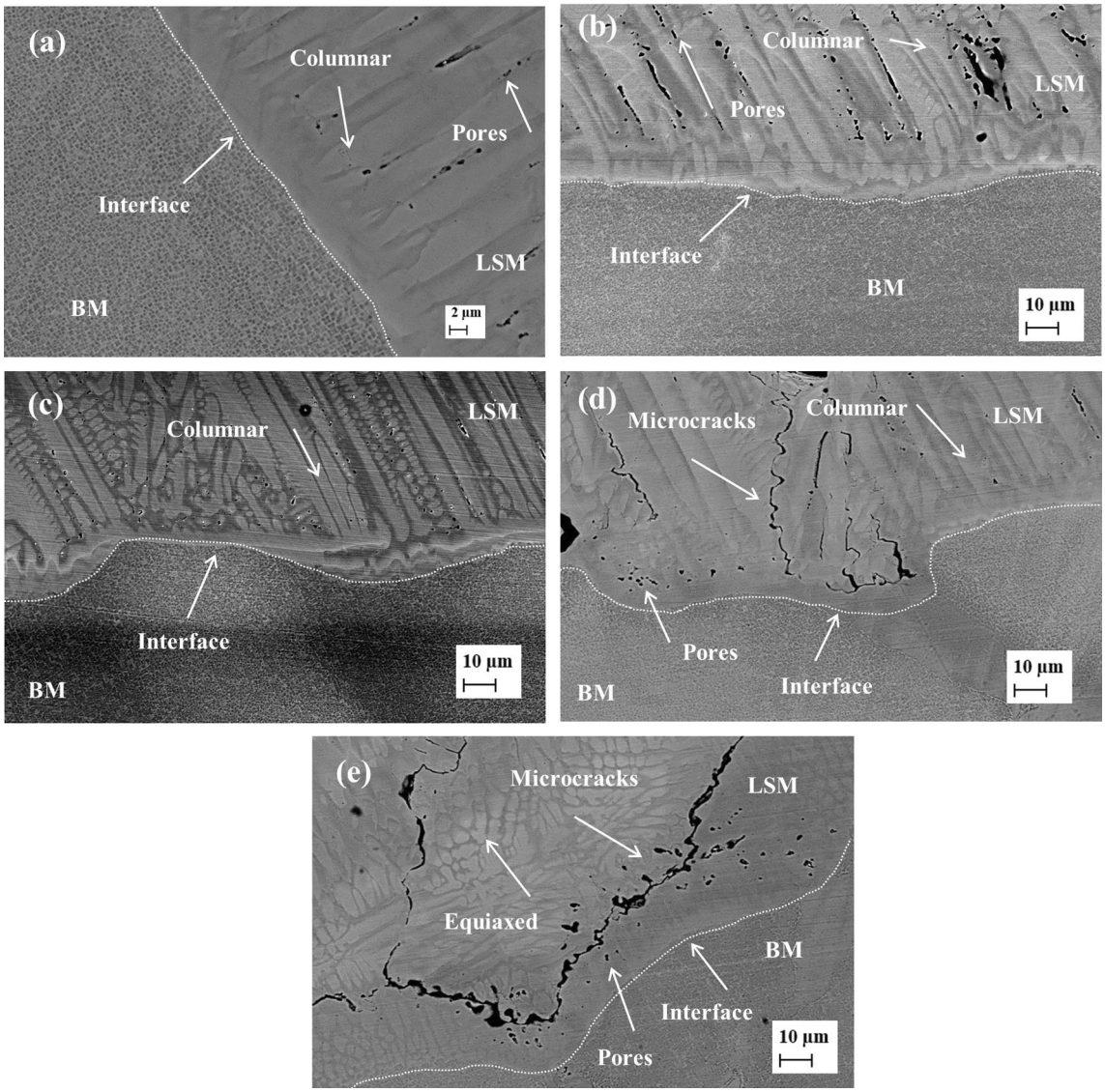

Fig. 6 SEM micrographs (2000 x) of the cross section of the LSM geoemtry at the inteface of a SX nickel-based superalloy under the laser power of (a) 500, (b) 750, (c) 1000, (d) 1250 and (e) 1500 W

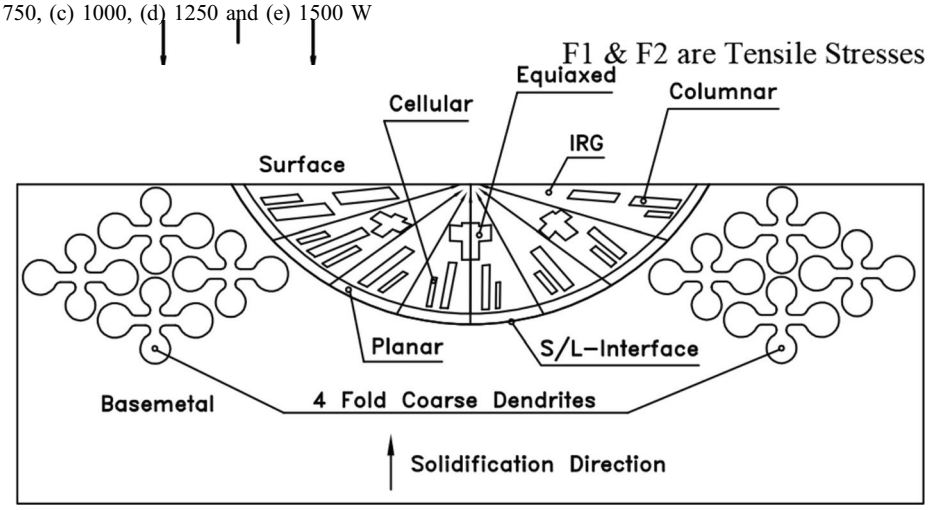

Fig. 7 Microstructural changes in the laser irradiated geometry of a SX nickel-based superalloy under CW fiber laser with laser power of 1 kW, scan speed of 5.5 mm/s and beam diameter of 1.2 mm (Ref 25). Printed with permission-email correspondence dated 06 June 2023

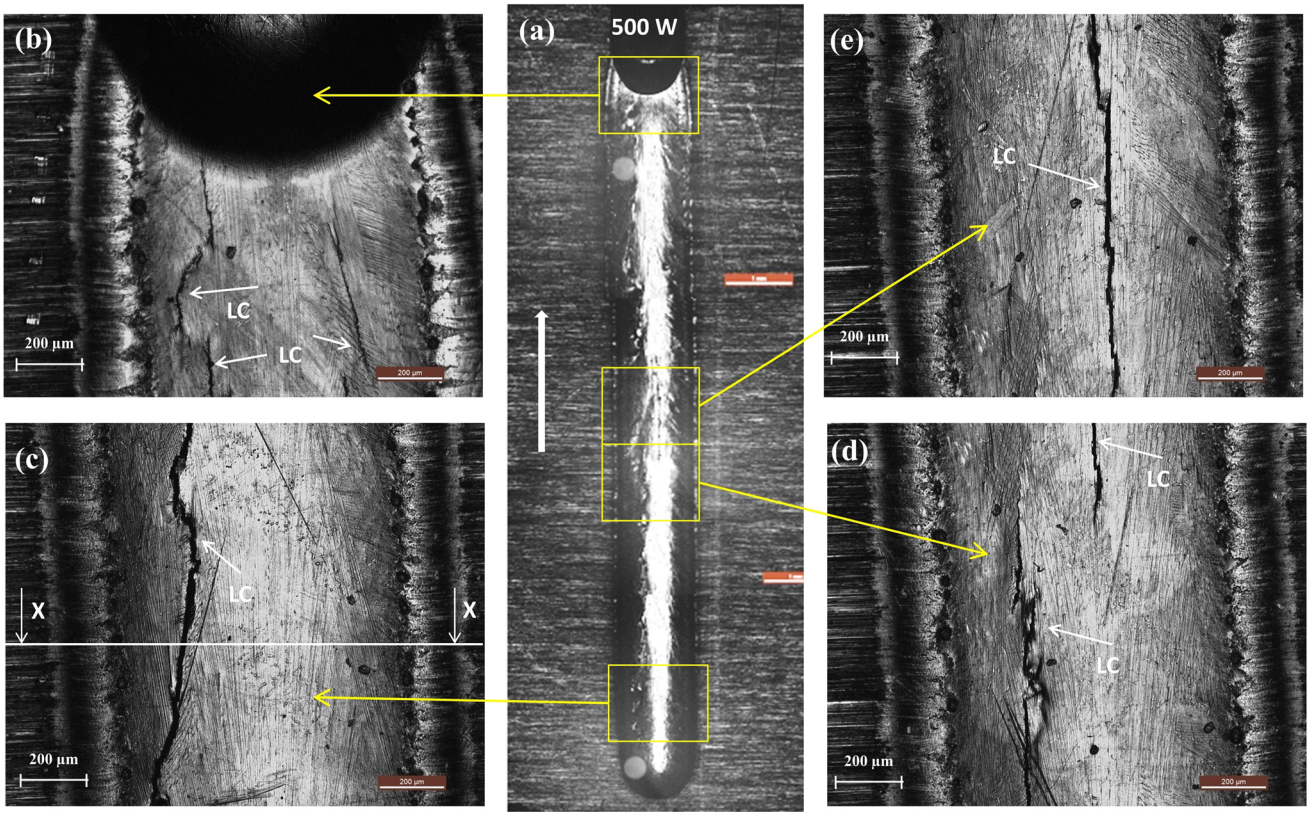

Fig. 8 Optical micrographs of the surface cracks (plan view) in the LSM region of the SX nickel-based superalloy at laser power of 500 W (a) total scan length under low magnification indicating the various locations for high magnification analysis, and magnified image (50 x) of (b) start zone, (c) middle 1 zone, (d) middle 2 zone, and (e) end zone

0.4 μm to 2 μm are visible mainly at inter-dendrite region (IDR) of the fine dendrites in the LSM geometry. The pores seem to have developed from the melting of eutectic compounds that prevailed in the BM at IDR.

3.2.2 LSM Interface. A high magnification (2000 x) SEM micrographs of the cross section of the LSM geometry at the interface under various laser powers are shown in Fig. 6(a), (b), (c), (d), and (e). Columnar dendrites are visible nearer to the interface due to the epitaxial growth of dendrites from the interface (heat sink) toward a point on the surface (heat source), except at a laser power of 1500 W. The interface consists of nodular dendrites under a laser power of 1500 W. The collapsed epitaxy at the highest laser power could be due to a change in the shape of the interface as the conduction mode changes to the transition mode. Dense microcracks and micropores are visible in the IDR at the interface. These micropores could grow into microcracks under higher laser powers.

The dendrites grow from the interface to the surface in planar to columnar and to equiaxed shapes in the LSM region under lower laser powers, these observations were corroborated by the author's earlier publication on laser irradiation experiments on a SX nickel-based superalloy by using a CW fiber laser (Ref 25). The microstructural changes that occur in the laser-irradiated geometry of a SX nickel-based superalloy under the laser scanning process are schematically shown in Fig. 7.

3.3 Crack Morphology

3.3.1 Surface Cracks. The magnified optical micrographs (50 x) of the LSM region at the lowest laser power are shown in Fig. 8. The start zone, middle 1, middle 2, and end zone of the laser scan are shown in Fig. 8(a), (b), (c), and (d), respectively. It is observed that a thick longitudinal crack (LC) initiates at the start zone and it propagates along the scan direction up to the middle 1 zone. A thin LC initiates at the middle of the scan length near the centerline and propagates near to the end zone. A few thin LCs formed near the end zone.

The magnified optical micrographs of the surface cracks in the LSM region at the laser power of 750 W are shown in Fig. 9. It is observed that a transverse crack (TC) gets initiated at the interface nearer to the start of the laser scan (Fig. 9b). It propagates toward the centerline of the LSM geometry

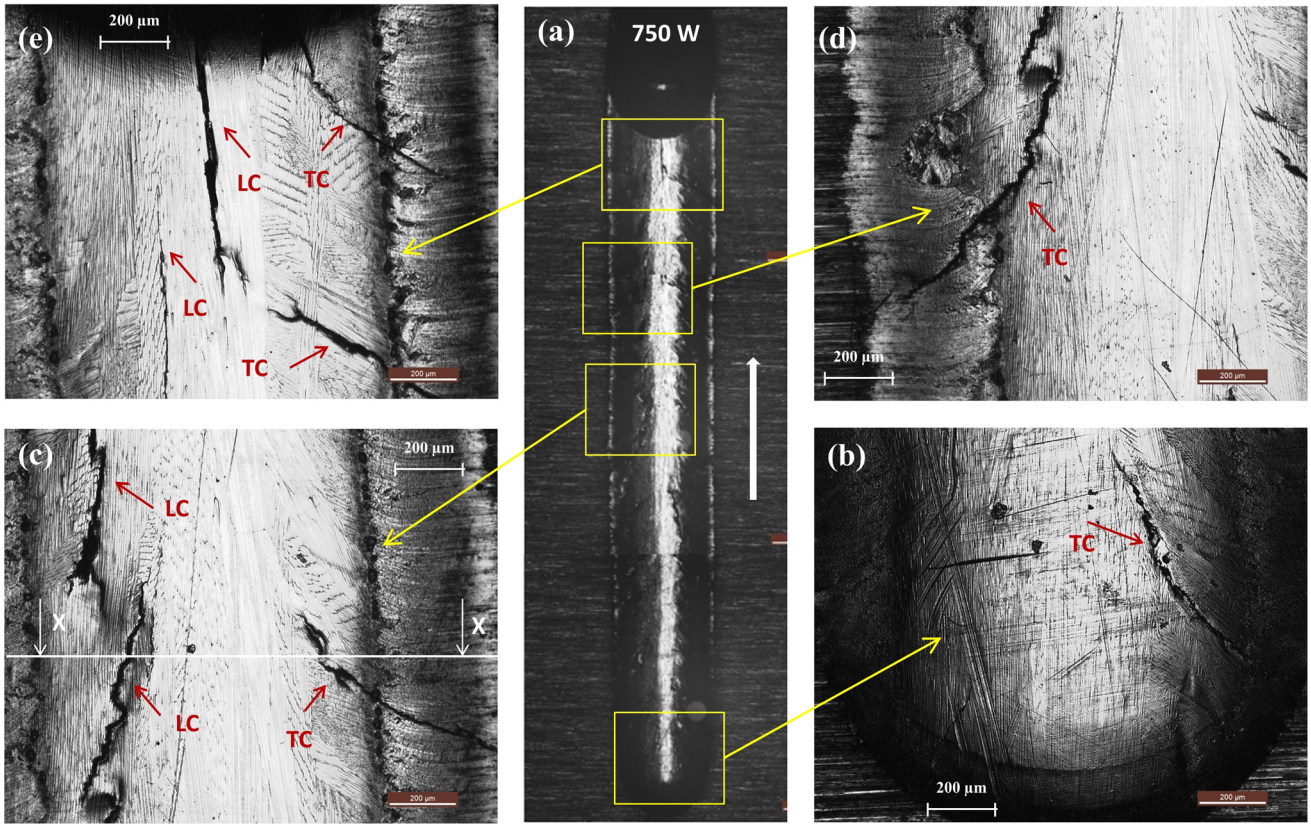

Fig. 9 Optical micrographs of the surface crack (plan view) in the LSM region of the SX nickel-based superalloy at laser power of 750 W (a) total scan length under low magnification indicating the various locations for high magnification analysis, and magnified image (50 x) of (b) start zone, (c) middle 1 zone, (d) middle 2 zone, and (e) end zone

diagonally, along the scan direction. The middle 1 zone (Fig. 9c) consists of a TC with multiple short LCs. The middle 2 zone (Fig. 9d) consists of multiple TCs and LC. The end zone consists (Fig. 9e) of multiple LCs and TCs. The cracks in the end zone are greater in numbers than in the start zone.

The magnified optical micrographs of the surface cracks in the LSM region at the intermediate laser power are shown in Fig. 10. It is observed that the start zone (Fig. 10b) consists of a longer LC along the centerline of the LSM and a shorter TC nearer to the interface. The middle 1 zone (Fig. 10c) consists of a longer TC. The middle 2 zone (Fig. 10d) consists of multiple TCs. The end zone (Fig. 10e) consists of multiple short TCs and an LC. The end zone consists of a larger number of cracks like a laser power of 750 W.

The magnified optical micrographs of the surface cracks in the LSM region at the laser power of 1250 W are shown in Fig. 11. It is observed that two LCs are initiated near to the centerline of LSM geometry at the start zone (Fig. 11b). The 1st one propagates along the scan direction up to the middle 2 zone and the 2nd one propagates up to the middle 1 zone (Fig. 11c). The middle 2 zone (Fig. 11d) consists of multiple TCs and a longer LC, and the LC propagates up to the end zone. The end zone (Fig. 11e) consists of multiple short TCs in addition to the LC, it originates in the middle 2 zone. A TC seems to have originated from the LC at the end of the laser scan.

The magnified optical micrographs of the surface cracks at various locations in the LSM region at the highest laser power are shown in Fig. 12. It is observed that the start zone (Fig. 12b) consists of a longer LC and two TCs. The LC seems to originate at the centerline of the LSM at the start of the laser scan. It propagates up to the end of the laser scan along the centerline. The thicker TC seems to originate from the LC near to the start of the laser scan and propagates diagonally to the interface in direction opposite to the scanning. A thinner TC exists at the end of the start zone, and it propagates to the interface and perpendicular to the scanning direction. The middle 1 zone (Fig. 12c) consists of a thicker TC in addition to the longer LC. The TC seems to originate at the interface, propagates diagonally along the scan direction, and gets joined the LC in the middle. The middle 2 zone (Fig. 12d) consists of

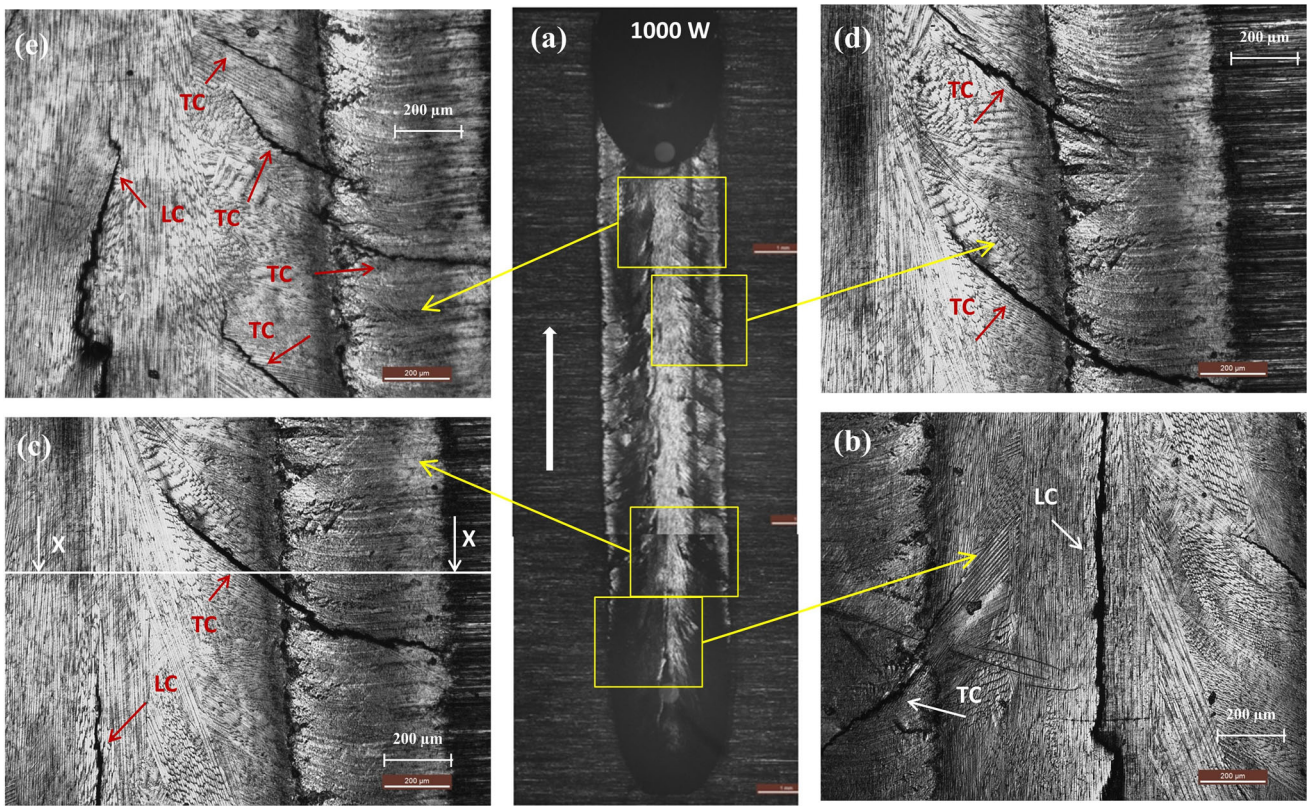

Fig. 10 Optical micrographs of the surface cracks (plan view) in the LSM region of the SX nickel-based superalloy at laser power of 1000 W (a) total scan length under low magnification indicating the various locations for high magnification analysis, and magnified image (50 x) of (b) start zone, (c) middle 1 zone, (d) middle 2 zone, and (e) end zone

no new cracks except the longer LC. The end zone (Fig. 12e) consists of two TCs along with the longer LC. A longer TC seems to originate at the interface and propagates diagonally along the scan direction. The shorter TC originates from the longer TC near to the centerline.

It can be concluded from the above observations that the lower laser powers result in LC, whereas the intermediate and higher laser powers result in both LC and TC. The LC is mainly formed near the centerline of the LSM, whereas the TC is mainly formed at a certain distance away from the centerline toward the interface. The end zone of LSM has a higher number of cracks than the start zone due to heat accumulation along the scan length. The TC at the intermediate laser power could not propagate up to the centerline, whereas the TC at higher laser power could propagate and form branched cracks. The formation of LC near the centerline could be due to tensile stresses along the width of the LSM region, whereas TC nearer to the interface could be due to the tensile stresses generated from heating loads along the scanning directions from the remelted regions. A schematic of the formation of LC and TC cracks under various laser powers is shown in Fig. 13.

The crack morphology was measured by the crack count and the crack width for estimating the intensity of cracking. The variations of the total crack count (sum of LC and TC) and maximum crack width on the top surfaces of the LSM region with the laser power are shown in Fig. 14. It is observed that the number of cracks increases up to a laser power of 1000 W and decreases thereafter. The crack width is around 30 μm size up to a laser power of 1000 W, and increases steeply to threefold at the laser power of 1500 W.

3.3.2 Cracking Beneath the Surface. The magnified views (1000 x) of a few LC and TC cracks in the cross section (the cutting line is shown with x-x in the figures of the surface crack subsection, 3.3.1) of the LSM geometry under various laser powers are shown in Fig. 15. The formation of dendrites adjacent to the crack region indicates that the cracks were formed after solidification. The LC propagates in a vertical

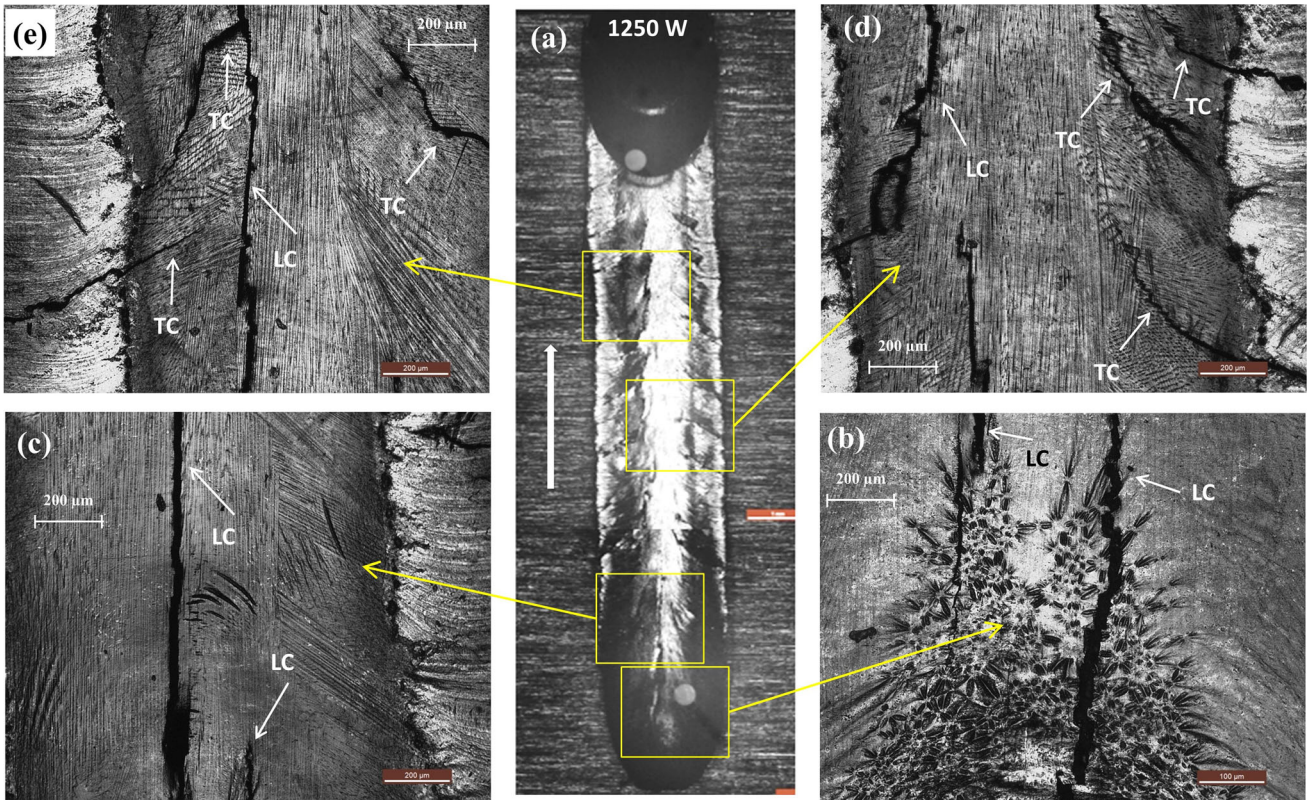

Fig. 11 Optical micrographs of the surface cracks (plan view) in the LSM region of the SX nickel-based superalloy at laser power of 1250 W (a) total scan length under low magnification indicating the various locations for high magnification analysis, and magnified image (50 x) of (b) start zone, (c) middle 1 zone, (d) middle 2 zone, and (e) end zone

direction, whereas the TC propagates in a zing-zag manner from the surface to the interface. The grain growth directions on the cracks are marked with white arrows in the figures showing that the dendrites near the cracks have multiple directions. The change in direction was higher for TC than LC. The change in growth direction results in the generation of strains. These strains could in turn lead to the formation of cracks.

The total crack length (TCL) in the LSM region was measured from the summation of individual crack lengths. The crack density was calculated as the ratio of TCL and LSM area. The details of the crack geometry such as the number of cracks, crack width, and TCL beneath the surface in the LSM as a function of laser power are presented in Fig. 16. It is observed that the crack count is the highest at the intermediate laser power and lowest at the highest laser power (Fig. 16a), whereas the average crack width is nearly the same at all laser powers except at the highest laser power (Fig. 16b). The TCL increases significantly with an increase in laser power from 500 W to 1000 W and it marginally varies thereafter (Fig. 16c). The observed larger error bars in the crack width for the LSM geometry with 1000 W could be due to the outlier from a wider crack width at the surface of a TC situated on the right side, and a narrower crack width at the surface of a TC situated on the left side (Fig. 15c). In comparison, the crack density exhibits a reverse trend with little variation up to the laser power of 1000 W and sharply decreases thereafter. The decrease in crack density under higher laser powers was due to the increase in the LSM area.

3.4 Elemental Chemical Analysis

The typical selected areas in the base metal (BM), LSM region and at the interface for the chemical analysis are shown in Fig. 17(a), (b), and (c). The segregation ratio (k) is the ratio of the measured composition and nominal composition. The segregation ratios of the alloying elements were calculated, and their averages were obtained. The average segregation ratios of the alloying elements in the LSM region, as well as at the

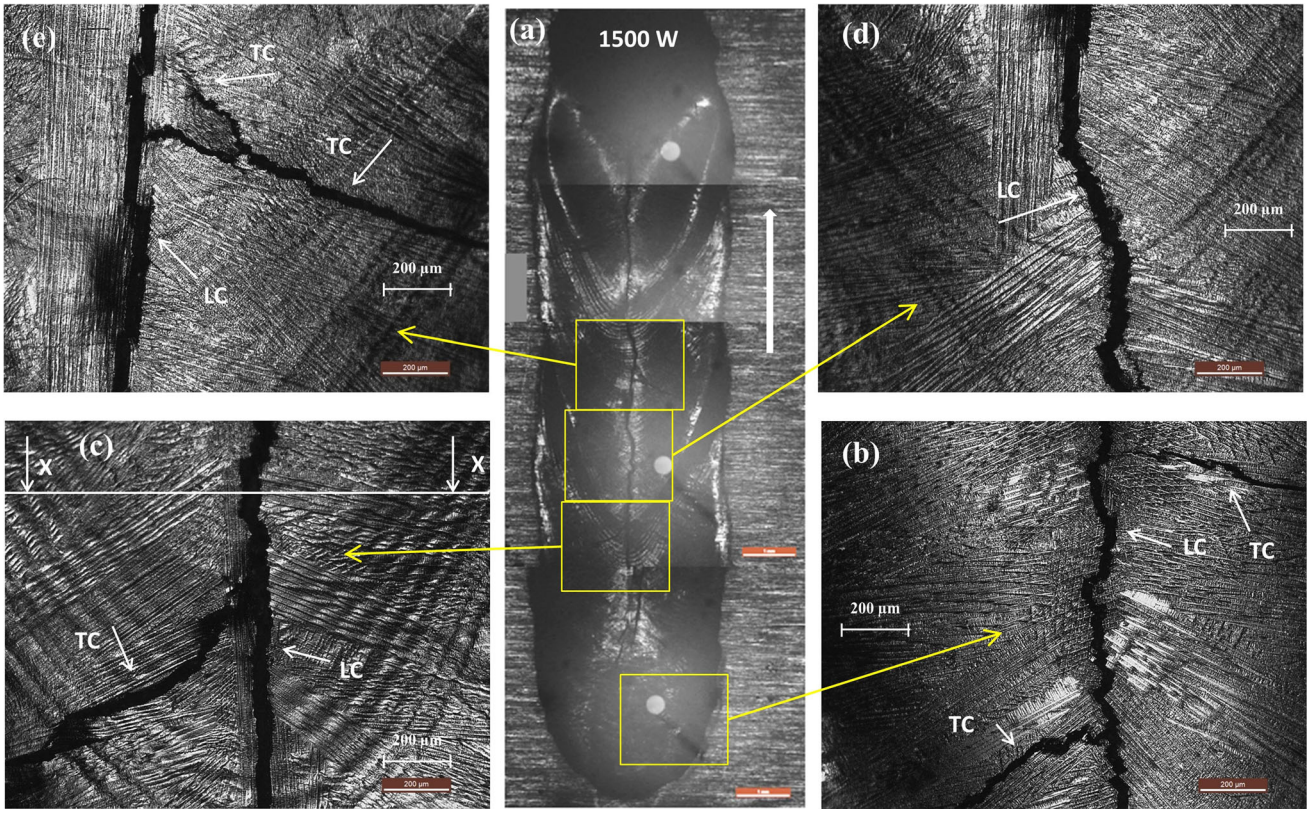

Fig. 12 Optical micrographs of the surface cracks (plan view) in the LSM region of the SX nickel-based superalloy at laser power of 1500 W (a) total scan length under low magnification indicating the various locations for high magnification analysis, and magnified image (50 x) of (b) start zone, (c) middle 1 zone, (d) middle 2 zone, and (e) end zone

interface and in the BM under varying laser powers are shown in Fig. 17(d). It is observed that the BM consists of a certain micro-segregation of W and Re elements from the dendritic core region, and Ti, Ta, and Al elements from the inter-dendrite region. The LSM region and the interface also follow a similar trend but with lower intensity.

Many research studies found that polycrystalline heat-resistant superalloys exhibit liquation cracking near the melt boundary and HAZ under remelting due to the formation of liquid film at the grain boundaries (Ref 26). SEM analysis revealed that a significant crack (crack length of 20 μm) was formed in the eutectic compound, which exists in the BM near the melt pool boundary. A high magnification (20000 x) SEM investigation revealed that solid metal deposits were present inside the crack (Fig. 18d). The elemental analysis was performed on the solid metal deposit by using the EDS technique to evaluate the chemical composition. The selected area of around 0.8 μm x 0.8 μm for the measurement is shown with a red color square in Fig. 18(d). The EDS spectrum of the solid deposit is shown in Fig. 18(e). The comparative results of the solid deposit along with the base metal are shown in Fig. 18(f). It is observed that the solid deposit consists of a higher chemical composition of Ta, Cr, and Mo elements. It could be a resolidified metallic phase formed from the eutectic compound.

3.5 Microhardness

It is known that the cracks weaken the material severely and reduce the strength of the alloy. The effect of microstructural changes in the LSM geometries at the non-cracked region on the surface hardness was evaluated by using Vickers micro-hardness measurement in the horizontal direction, it was parallel to the surface at 0.2 mm depth and vertical direction, that was perpendicular to the surface nearer to the centerline up

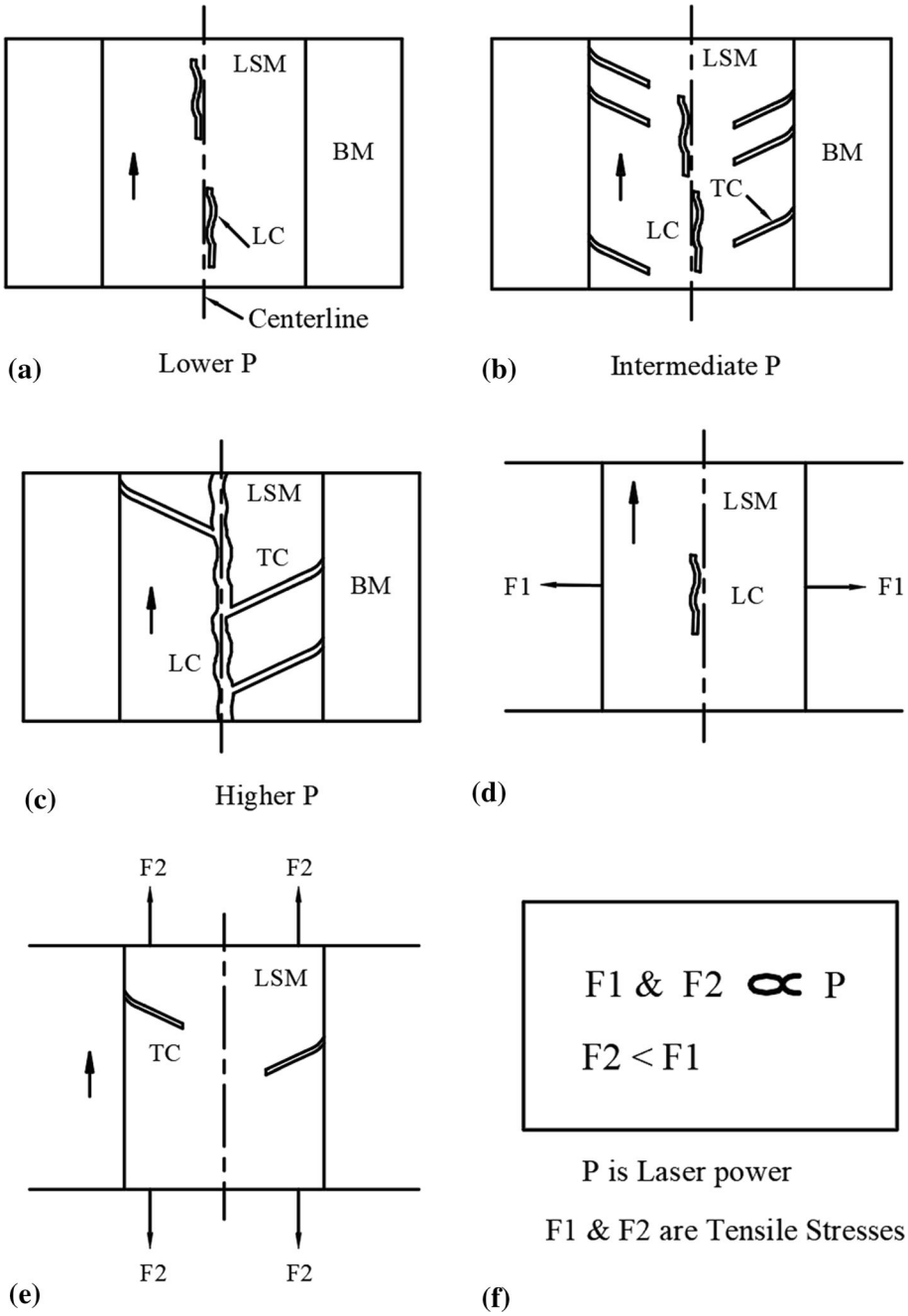

Fig. 13 Schematic of the formation of longitudinal and transvers cracks in the top surface of the LSM region, (a) LC at the lower laser power, (b) LC and TC at the intermediate laser power, (c) branched cracks at the higher laser power, (d) tensile stresses on LC along the scan width, (e) tensile stresses on TC along the scan direction, and (f) relationship of the tensile stresses of LC and TC in the LSM region

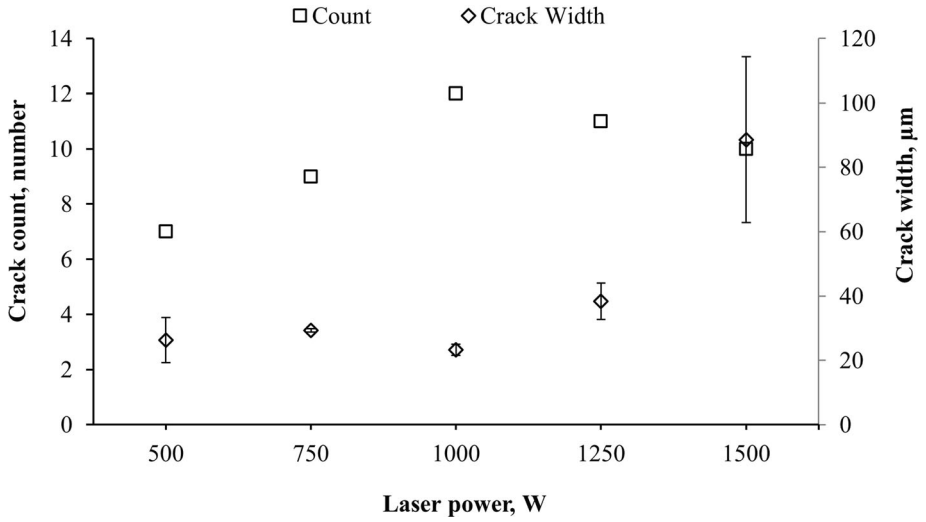

Fig. 14 Variation of crack count and crack width of the surface cracks in the LSM region of a SX nickel-based superalloy with laser power

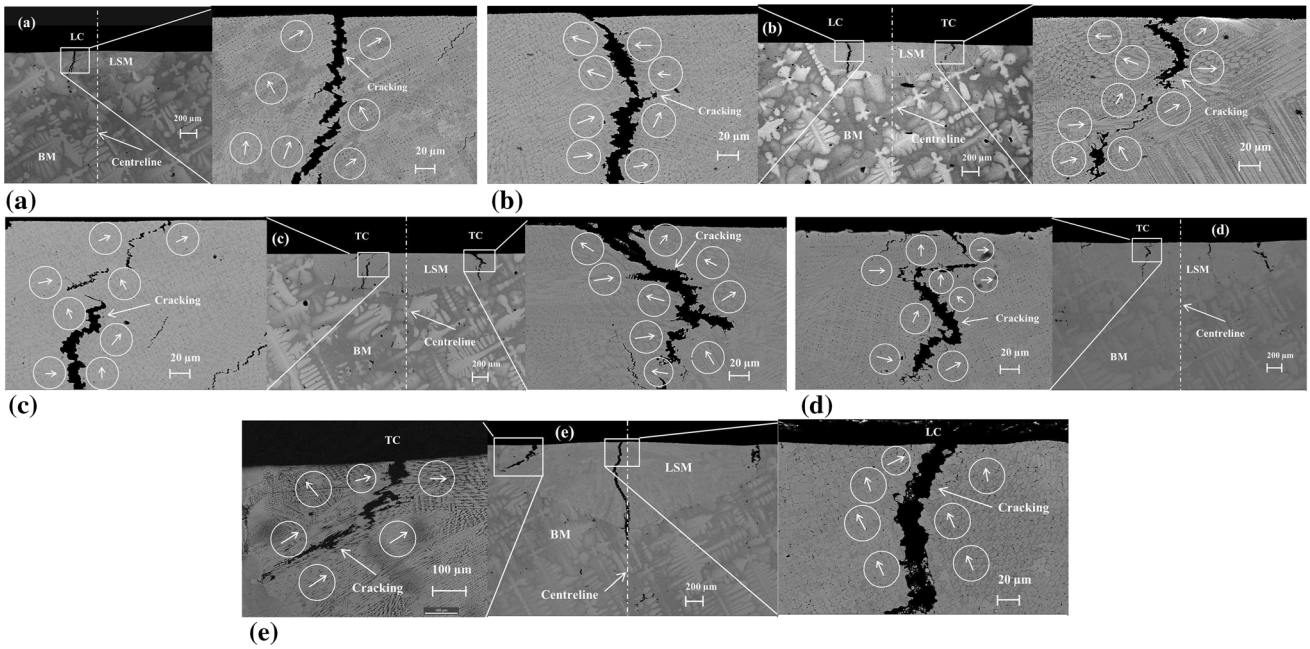

Fig. 15 Magnified (1000 x) SEM micrographs of the LC and TC beneath the surface in the LSM geometry of a SX nickel-based superalloy along with the grain growth directions (white arrows) corresponding to the laser power of (a) 500, (b) 750, (c) 1000, (d) 1250, and (e) 1500 W

to 2.0 mm depth with a spacing of 0.2 mm as per ASTM standard E384-17 (Ref 27). A schematic of the microhardness measurement scheme, in the LSM geometry in both horizontal and vertical directions is shown in Fig. 19(a). The Vickers microhardness indentations (letters ***a*** to ***g***) along the horizontal direction on the LSM geometry with 750 W laser power are shown in Fig. 19(b). The Vickers microhardness indentations (numeric ***1*** to ***10***) along the vertical direction on the LSM geometry, made using 1000 W laser power are shown in 19(*c*).

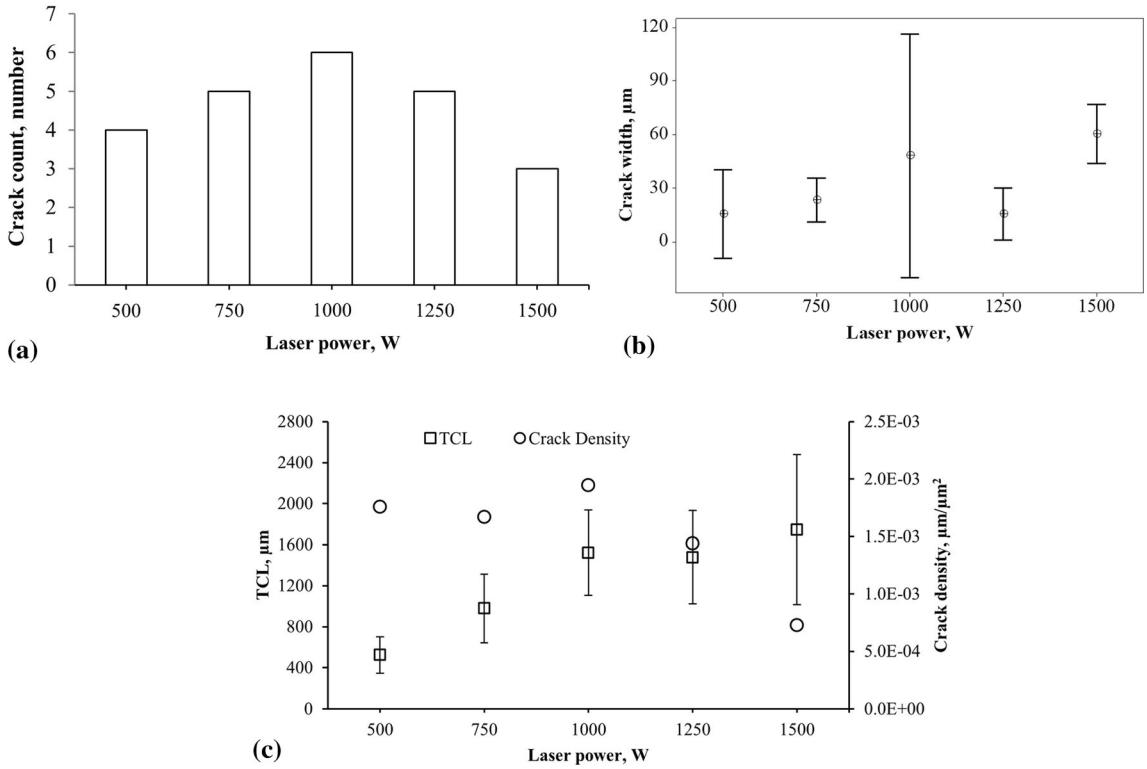

Fig. 16 The crack geometry beneath the surface in the LSM region (a) number of cracks, (b) crack width, and (c) TCL and crack density as a function of the laser power

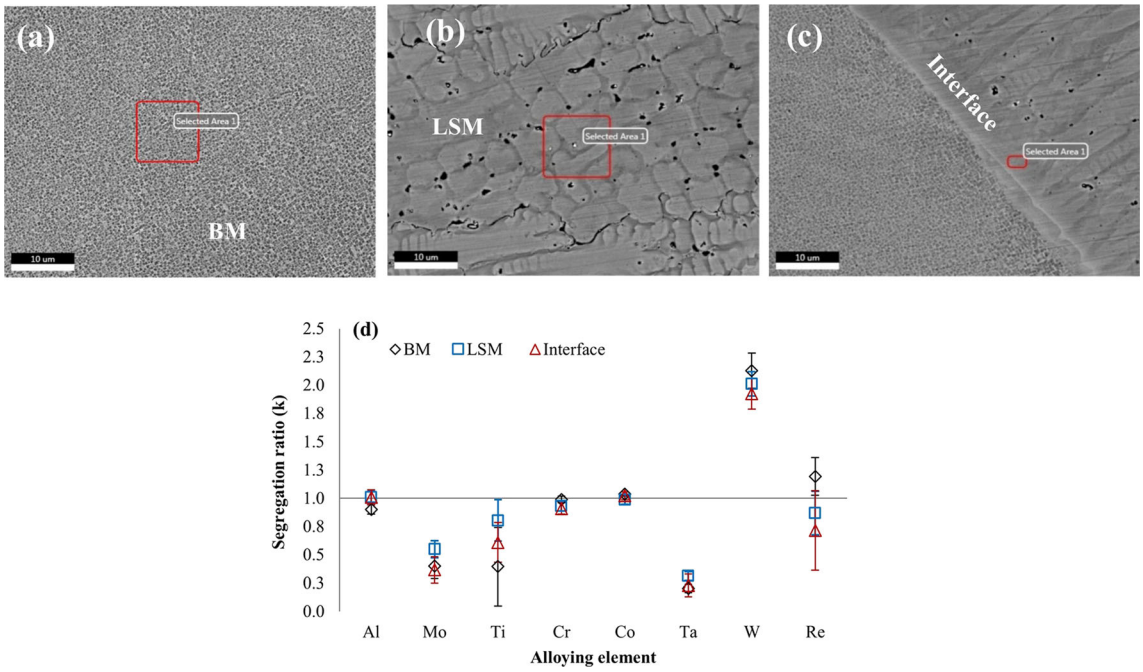

Fig. 17 Elemental chemical analysis, (a) identification location at BM, (b) LSM region and (c) interface, and (d) average segregation ratio of the alloying elements in the three locations along with error bars

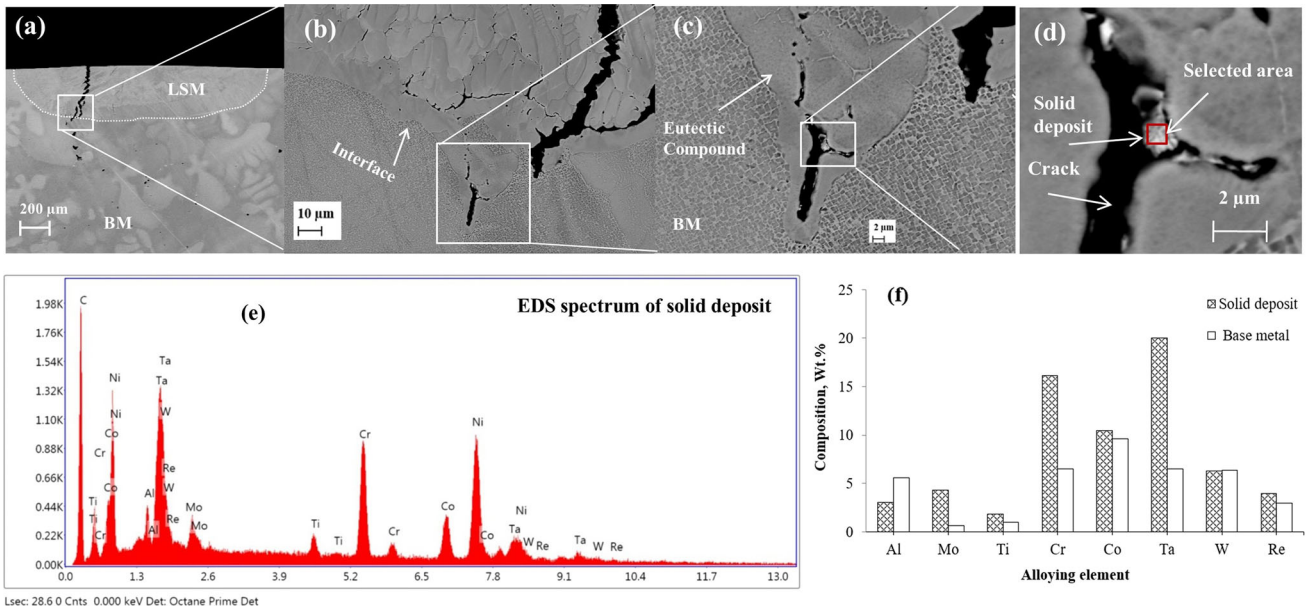

Fig. 18 Elemental analysis of the solid metal deposit inside the crack at the eutectic compounds nearer to the interface, (a) to (d) SEM micrographs for locations of EDS measurement, (e) EDS spectrum of elemental analysis of the solid deposit, and (f) comparative results of the elemental composition of the solid metal deposit along with the base metal

The Vickers microhardness results of the LSM geometry at a depth of 0.2 mm along the horizontal direction are shown in Fig. 20(a). The Vickers microhardness results of the LSM geometry beneath the surface along the vertical direction are shown in Fig. 20(b). It is observed that the unexposed BM adjacent to the LSM geometry in Fig. 20(a) as well as the unexposed BM below the LSM geometry in Fig. 20(b) has lesser scatter than the LSM geometry. A comparison results of the microhardness of the LSM geometry along with the unexposed BM, as a function of laser power are shown in Fig. 20(c). It is observed that the average microhardness in the BM ranges from 431 to 448 VHN, whereas the microhardness in the LSM geometry ranges from 394 to 434 VHN. The hardness in the LSM geometry increases with an increase in laser power. The hardness in the equiaxed dendritic region at the central region of the LSM geometry has comparatively higher hardness than the interface region. The lower hardness in the interface region could be due to the existence of dense micropores and microcracks. The increase in hardness with an increase in laser power could be due to an increase in dendrite size. The considerably higher hardness in the LSM region at higher power is attributed to the existence of many equiaxed dendrites.

4. Conclusion

Laser surface modification (LSM) was carried out in a second-generation single-crystal nickel-based superalloy, CMSX-4 alloy. A continuous wave fiber laser with laser power ranging from 500 W to 1500 W was used in an argon gas shielding atmosphere under the conductive mode of heat penetration. The results of the experimental investigation revealed the following major findings:

- The LSM geometry under lower laser powers consists of smooth surfaces and flat interfaces, whereas the geometry under higher powers consists of rough surfaces and curved interfaces due to the instabilities in the melt pool. At lower laser power operating in single mode, the cross section of the LSM geometry was observed to be a semi-elliptical shape, whereas at higher laser powers operating in multi-mode the geometries were observed to be a top-hat shape.
- The LSM geometry consists of fine dendrites of around 10 μm with various morphologies due to rapid solidification. The size reduction was about 30 times when compared with the base metal. The dendrite size increases with an increase in laser power except at high laser

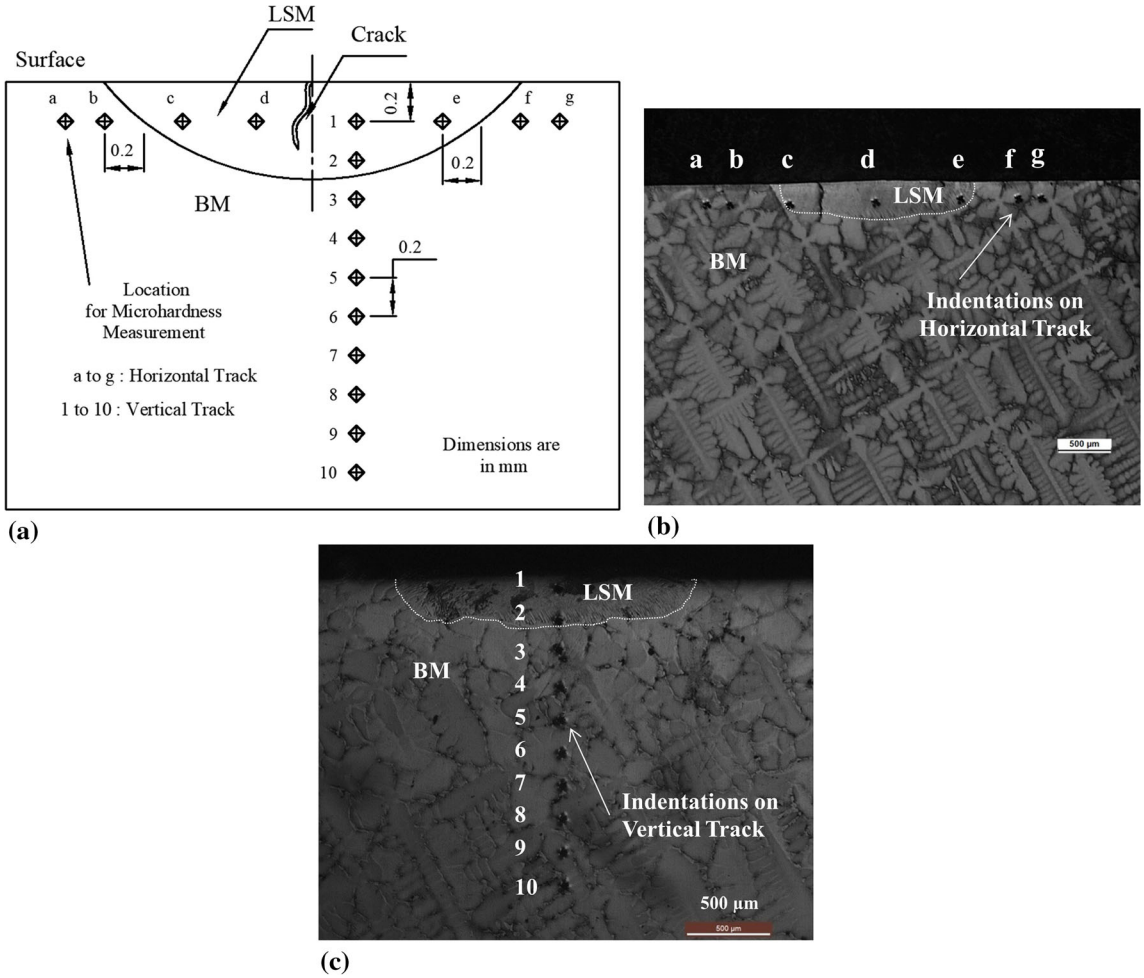

Fig. 19 Vickers microhardness measurement in the LSM geometries under various laser powers, (a) a schematic diagram of the microhardness measurement scheme, (b) Vickers microhardness indentations along the horizontal direction at a depth of 0.2 mm on the LSM geometry made with 750 W laser power, and (c) Vickers microhardness indentations along the vertical direction beneath the surface of the LSM geometry made with 1000 W laser power

power.

- Pores of size ranging from 0.4 to 2 μm are formed at the inter-dendrite region in the LSM geometry. These pores transformed into microcracks under higher laser powers.
- The LSM geometry consists of longitudinal cracks (LC) and transverse cracks (TC) along the scanning direction. The LC are formed near the centerline at lower laser power, whereas the TC are formed at a faraway distance from the centerline at higher laser power. The LC consists of vertical cracking, whereas TC consists of zig-zag cracking beneath the depth from the surface to the interface. The crack regions consist of fully formed dendrites with various orientations. The thermal stress along with the strain induced by dendrite growth directions could be the reason for cracking.
- Resolidified metal deposits are observed inside the crack at eutectic compounds.
- The LSM geometry consists of significantly lower hard-

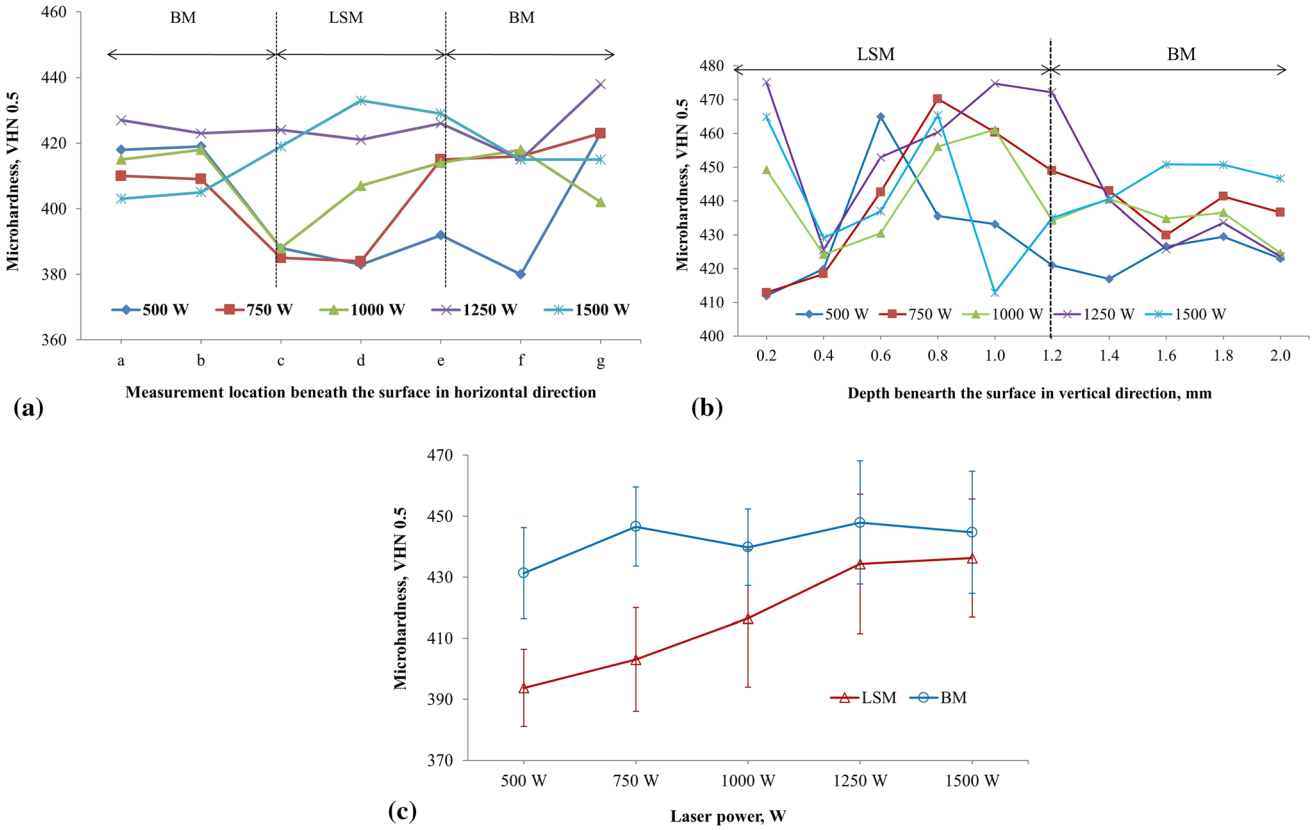

Fig. 20 Microhardness of the LSM geometry under various laser powers, (a) results in the horizontal direction, (b) results in the vertical direction, and (c) comparative results of the LSM geometries as a function of laser powers along with the base metal

ness than the base metal due to the formation of laser-induced surface defects such as micropores, microcracks, stray grains, and solidification cracks in addition to the dissolution of strengthening precipitates under rapid melting and solidification.

Thus, the LSM resulted in a decrease in the surface strength of a single-crystal nickel-based superalloy. The investigation found that the optimum combination of laser power and scan speed was 1000 W and 5.5 mm/s, respectively, to get the maximum surface damage. The reduced strength by the surface damage will significantly improve the machinability of the superalloy.

Acknowledgments

The authors wish to extend their gratitude to Director, DMRL for his encouragement. The authors are thankful to Prof. Deepak Marla, IIT Bombay for his valuable insights and discussions. The authors also express their gratitude to the officers and staff of DSG, MEG, SFAG, and EMG of DMRL for their support. Additionally, they thank Dr. P. Mastanaiah, Scientist-F, SFD of DOE, DRDL and his team, for their support in carrying out the LSM experiments. Finally, the authors acknowledge the financial assistance provided by Defence Research and Development Organization (DRDO), New Delhi.

References

1. T.M. Pollock and S. Tin, Nickel-Based Superalloys for Advanced Turbine Engines: Chemistry, Microstructure, and Properties, *J. Propuls. Power*, 2006, **22**, p 361–374.
2. R.C. Roger, *The Superalloys: Fundamentals and Applications*, Cambridge University Press, Cambridge, 2006
3. R. Arunachalam and M.A. Mannan, Machinability of Nickel-Based High Temperature Alloys, *Mach. Sci. Technol.*, 2000, **4**(1), p 127–168.
4. W. Akhtar, J. Sun, P. Sun, W. Chen, and Z. Saleem, Tool Wear Mechanisms in the Machining of Nickel Based Super-Alloys: A Review, *Front. Mech. Eng.*, 2014, **9**(2), p 106–119.
5. M. Anderson, R. Patwa, and Y.C. Shin, Laser-Assisted Machining of Inconel 718 with an Economic Analysis, *Int. J. Mach. Tools Manuf.*, 2006, **46**(14), p 1879–1891.
6. A. Onyszko, K. Kubiak, and J. Sieniawski, Turbine Blades of the Single Crystal Nickel Based CMSX-6 Superalloy, *J. Achiev. Mater. Manuf. Eng.*, 2009, **32**(1), p 66–69.
7. P.K. Samantaroy, S. Girija, R. Kaul, and U.K. Mudali, Enhancement of Corrosion Resistance of Nickel Based Superalloys by Laser Surface Melting, *Surface Eng.*, 2013, **29**(7), p 522–530.
8. S. Ruppik, F. Becker, F.-P. Grundmann, W. Rath, and U. Hefter, High-Power Disk and Fiber Lasers: A Performance Comparison, *Solid State Lasers XXI: Technol. Devices*, 2012, **8235**, p 82350V.

9. T.D. Anderson, J.N. DuPont, and T. DebRoy, Origin of Stray Grain Formation in Single-Crystal Superalloy Weld Pools from Heat Transfer and Fluid Flow Modeling, *Acta Mater.*, 2010, **58**(4), p 1441–1454.
10. Y.J. Liang and H.M. Wang, Origin of Stray-Grain Formation and Epitaxy Loss at Substrate during Laser Surface Remelting of Single-Crystal Nickel-Base Superalloys, *Mater. Des.*, 2016, **102**, p 297–302. https://doi.org/10.1016/j.matdes.2016.04.051
11. A. Basak, S. Holenarasipura Raghu, and S. Das, Microstructures and Microhardness Properties of CMSX-4® Additively Fabricated Through Scanning Laser Epitaxy (SLE), *J. Mater. Eng. Perform.*, 2017, **26**(12), p 5877–5884.
12. B. Rottwinkel, C. Nölke, S. Kaierle, and V. Wesling, Laser Cladding for Crack Repair of CMSX-4 Single-Crystalline Turbine Parts, *Lasers Manuf. Mater. Process.*, 2017, **4**(1), p 13–23.
13. Z. Zhou, L. Huang, Y. Shang, Y. Li, L. Jiang, and Q. Lei, Causes Analysis on Cracks in Nickel-Based Single Crystal Superalloy Fabricated by Laser Powder Deposition Additive Manufacturing, *Mater. Des.*, 2018, **160**, p 1238–1249. https://doi.org/10.1016/j.matdes.2018.10.042
14. R. Korsmik, O. Klimova-Korsmik, E. Valdaytseva, and I. Udin, Investigation of Cracking Causes during Multi-Pass Laser Cladding of Heat-Resistant Single Crystal Nickel Alloy, *Procedia CIRP*, 2020, **94**, p 314–319. https://doi.org/10.1016/j.procir.2020.09.059
15. K. Harris, G.L. Erickson, R.E. Schwer, F.D.J., and W.J.R. "Process and Alloy Optimization for CMSX-4 Superalloy Single Crystal Airfoils High Temperature Materials for Power Engineering," *Proc. Cost Conf. Liege 24-26 September ed Bachelet E. et al (ed)*, 1990
16. A. Szczotok and R. Przeliorz, Phase Transformations in CMSX-4 Nickel-Base Superalloy, *IOP Conf. Ser. Mater. Sci. Eng.*, 2012, **35**(1), p 012005.
17. M.S.A. Karunaratne, S. Kyaw, A. Jones, R. Morrell, and R.C. Thomson, Modelling the Coefficient of Thermal Expansion in Ni-Based Superalloys and Bond Coatings, *J. Mater. Sci.*, 2016, **51**(9), p 4213–4226.
18. T. Matsushita, H.J. Fecht, R.K. Wunderlich, I. Egry, and S. Seetharaman, Studies of the Thermophysical Properties of Commercial CMSX-4 Alloy, *J. Chem. Eng. Data.*, 2009, **54**(9), p 2584–2592.
19. K. Harris, B.W. Jacqueline, Improved Single Crystal Superalloys, CMSX-4 and CMSX-486, in: Green, K.A., Pollock, T.M., Harada, H., Howson, T.E., Reed, R.C., Schirra, J.J., Walston, S., (Eds.), Superalloys 2004, TMS, pp. 45- 52
20. Rofin Fiber Laser System, FL-010 operating manual, 2014. Coherent, Inc. Santa Clara, USA
21. C. Qiu, C. Panwisawas, M. Ward, H.C. Basoalto, J.W. Brooks, and M.M. Attallah, On the Role of Melt Flow into the Surface Structure and Porosity Development during Selective Laser Melting, *Acta Mater.*, 2015, **96**, p 72–79.
22. W.M. Steen and J. Mazumder, *"Laser Material Processing: Fourth Edition", Laser Material Processing*, 4th ed. Springer, London, 2010
23. S. Gobbi, L. Zhang, J. Norris, K.H. Richteff, and J.H. Loreau, High Powder CO2 and Nd-Yag Laser Welding of Wrought Inconel 718, *J. Mater. Process Technol.*, 1996, **56**, p 333–345.
24. N.J. Grant, "Rapid-Solidification-III-Mehrabian-Cohen-83-2758," Claitor's Publication Division, 1978, p 1–712
25. S.R. Nandam, A. Venugopal Rao, A.A. Gokhale, and S.S. Joshi, Experimental Study on Laser-Induced Surface Damage of a Single-Crystal Nickel-Based Superalloy Under Continuous Wave Fiber Laser Scanning Process, *J. Eng. Mater. Technol.*, 2022 https://doi.org/10.1115/1.4054228
26. K.R. Vishwakarma, N.L. Richards, and M.C. Chaturvedi, Microstructural Analysis of Fusion and Heat Affected Zones in Electron Beam Welded ALLVAC® 718PLUS™ Superalloy, *Mater. Sci. Eng., A*, 2008, **480**(1–2), p 517–528.
27. Standard Test Method for Microindentation Hardness of Materials, E 384, ASTM International, 2017, doi:https://doi.org/10.1520/E0384-17